Optimizing calibration settings for accurate water equivalent path length assessment using flat panel proton radiography

Seller Oria, Carmen; Guterres Marmitt, Gabriel; Free, Jeffrey; Langendijk, Johannes A; Both, Stefan; Knopf, Antje C; Meijers, Arturs

Published in:
Physics in Medicine and Biology

DOI:
10.1088/1361-6560/ac2c4f

NOTE • OPEN ACCESS

Optimizing calibration settings for accurate water equivalent path length assessment using flat panel proton radiography

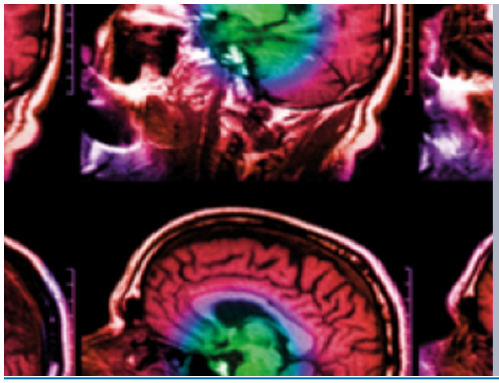

IOP Publishing Phys. Med. Biol. 66 (2021) 21NT02 https://doi.org/10.1088/1361-6560/ac2c4f

Physics in Medicine & Biology

IPEM Institute of Physics and Engineering in Medicine

NOTE

Optimizing calibration settings for accurate water equivalent path length assessment using flat panel proton radiography

Carmen Seller Oria*, Gabriel Guterres Marmitt, Jeffrey Free, Johannes A Langendijk, Stefan Both, Antje C Knopf and Arturs Meijers

Department of Radiation Oncology, University Medical Center Groningen, University of Groningen, The Netherlands

* Author to whom any correspondence should be addressed.

E-mail: c.seller.oria@umcg.nl

Keywords: proton radiography, flat panel detector, calibration, range uncertainties, adaptive proton therapy, water equivalent path length

Supplementary material for this article is available online

OPEN ACCESS

RECEIVED
14 May 2021

REVISED
27 September 2021

ACCEPTED FOR PUBLICATION
1 October 2021

PUBLISHED
21 October 2021

Abstract

Objective: Proton range uncertainties can compromise the effectiveness of proton therapy treatments. Water equivalent path length (WEPL) assessment by flat panel detector proton radiography (FP-PR) can provide means of range uncertainty detection. Since WEPL accuracy intrinsically relies on the FP-PR calibration parameters, the purpose of this study is to establish an optimal calibration procedure that ensures high accuracy of WEPL measurements. To that end, several calibration settings were investigated. Approach: FP-PR calibration datasets were obtained simulating PR fields with different proton energies, directed towards water-equivalent material slabs of increasing thickness. The parameters investigated were the spacing between energy layers (ΔE) and the increment in thickness of the water-equivalent material slabs (ΔX) used for calibration. 30 calibrations were simulated, as a result of combining $\Delta E = 9, 7, 5, 3, 1$ MeV and $\Delta X = 10, 8, 5, 3, 2, 1$ mm. FP-PRs through a CIRS electron density phantom were simulated, and WEPL images corresponding to each calibration were obtained. Ground truth WEPL values were provided by range probing multi-layer ionization chamber simulations on each insert of the phantom. Relative WEPL errors between FP-PR simulations and ground truth were calculated for each insert. Mean relative WEPL errors and standard deviations across all inserts were computed for WEPL images obtained with each calibration. Main results: Large mean and standard deviations were found in WEPL images obtained with large ΔE values ($\Delta E = 9$ or 7 MeV), for any ΔX. WEPL images obtained with $\Delta E \leqslant 5$ MeV and $\Delta X \leqslant 5$ mm resulted in a WEPL accuracy with mean values within $\pm 0.5\%$ and standard deviations around 1%. Significance: An optimal FP calibration in the framework of this study was established, characterized by $3\text{ MeV} \leqslant \Delta E \leqslant 5\text{ MeV}$ and $2\text{ mm} \leqslant \Delta X \leqslant 5$ mm. Within these boundaries, highly accurate WEPL acquisitions using FP-PR are feasible and practical, holding the potential to assist future online range verification quality control procedures.

Introduction

Range probing and proton radiography (PR) have been proposed as tools to detect and mitigate sources of range uncertainty (Mumot *et al* 2010). Based on the principle that the same particle is used for treatment and for imaging, PR enables a direct measurement of relative stopping power of tissues, overcoming the uncertainties arising from the conversion of CT numbers into relative stopping power (Schneider and Pedroni 1994, Schneider *et al* 2005, Knopf and Lomax 2013, Doolan *et al* 2015).

PR solutions, classified as list mode or integration detector configurations, were first developed in the context of double scattering proton therapy systems (Poludniowski *et al* 2015). List mode detector configurations are composed of upstream and/or downstream particle trackers, as well as a residual energy detector (Talamonti *et al* 2010, Johnson 2018). Integrating systems rely on a single detector such as diode arrays

(Gottschalk *et al* 2011, Testa *et al* 2013, Doolan *et al* 2015), scintillators with charge-coupled devices (Zygmanski *et al* 2000, Ryu *et al* 2008), or flat panels (FP) (Jee *et al* 2017a, Zhang *et al* 2018), which are typically calibrated to the water equivalent path length (WEPL) experimentally or via Monte Carlo simulations (Poludniowski *et al* 2015, Würl *et al* 2020). Given the growing prevalence of pencil beam scanning over double scattering systems, new PR integrating solutions compatible with pencil beam scanning were proposed (Mumot *et al* 2010, Telsemeyer *et al* 2012, Bentefour *et al* 2016).

Multiple studies have shown the suitability of PR for range verification with a multi-layer ionization chamber (MLIC-PR), which measures the integral depth-dose profiles of pencil beams (Mumot *et al* 2010, Farace *et al* 2016b). MLIC-PR enabled the detection of patient misalignments, range uncertainty assessment in different types of tissues, as well as *in vivo* range verification in head and neck cancer patients (Farace *et al* 2016b, Hammi *et al* 2018, Meijers *et al* 2021).

Other investigations with pencil beam scanning systems focus on PR imaging with flat panel detectors (FP-PR), which provide dose measurements in a two-dimensional detector array and offer larger readout areas with respect to MLIC. The WEPL of proton beams can be obtained using energy-resolved dose functions (ERDFs), first proposed by Bentefour *et al* as a solution to measure WEPL by FP-PR with pencil beam scanning systems. An ERDF represents the change in the FP signal as a function of different initial pencil beam energies composing the PR field (Bentefour *et al* 2016). The WEPL can be retrieved by comparing the ERDFs obtained from a PR acquisition against a set of calibrated ERDFs with slabs of known water equivalent thickness (Bentefour *et al* 2016, Huo *et al* 2019, Alaka *et al* 2020, Harms *et al* 2020).

WEPL obtaining by means of FP-PR using ERDFs was investigated *in silico* and verified experimentally with an electron density phantom, achieving relative stopping power accuracy below 1.5% *in silico* and 2.65% experimentally (Huo *et al* 2019, Harms *et al* 2020). For a head and neck phantom, FP-PR simulations were performed, and FP-PR image acquisitions were evaluated qualitatively (Huo *et al* 2019, Harms *et al* 2020). Even though WEPL accuracy relies intrinsically on the sparseness of the FP calibration dataset (Harms *et al* 2020), research up to date has not yet provided an optimal FP calibration procedure, which is essential for accurate WEPL assessment using FP-PR. In this work, WEPL accuracy was assessed *in silico* as a function of different calibration parameters with the purpose to find an optimal setting for FP calibration.

Materials and methods

FP calibration settings

In this study, different calibration settings were explored. Each simulated calibration contained a collection of ERDFs obtained by repeatedly delivering a PR field, composed of multiple energy layers, towards water-equivalent material slabs of increasing thickness. The calibration parameters subject to investigation were the spacing between energy layers in the PR field (ΔE), and the slab thickness increments (ΔX).

Thirty calibration settings were generated, as a result of exploring five different spacings between energy layers ($\Delta E = 9, 7, 5, 3$ and 1 MeV) combined with six different slab thickness increments ($\Delta X = 10, 8, 5, 3, 2, 1$ mm).

FP-PR simulations were performed using openREGGUI (openreggui.org) (Farace *et al* 2016b, Deffet *et al* 2017), with MCsquare as the Monte Carlo dose engine (Souris *et al* 2016), which enabled dose calculations with an isotropic dose grid of 1 mm in all directions. Three water blocks along the beam path (z-axis) were simulated (see figure 1), representing a range shifter (40 mm of thickness), slabs of varying thickness (up to 80 mm) and a FP detector (5 mm of thickness, (Huo *et al* 2019)). All simulations were performed with PR fields covering an area of 30×30 cm^2 at the isocenter in the x–y plane, with a spot spacing of 5 mm, delivered at initial energies ranging from 70 to 225 MeV, from a gantry angle of 270 degrees.

For each energy layer in the PR field, the FP signal was extracted by integrating the FP dose along the beam direction (over the z-axis), thus obtaining a two-dimensional array in the x–y plane corresponding to the FP signal. For the calibration datasets, the FP signal assigned to each energy layer and slab thickness, e.g. each data point in every ERDF, was obtained after averaging the FP signal over all the pixels covered by the PR field in the x–y plane. Figure 2 shows two exemplary calibration datasets, the first one is composed of 41 ERDFs ($\Delta X = 2$ mm and $\Delta E = 3$ MeV), and the second one contains 9 ERDFs ($\Delta X = 10$ mm and $\Delta E = 9$ MeV).

WEPL obtained via FP-PR

In order to evaluate the WEPL accuracy achievable with each calibration setting, FP-PR simulations were performed using an electron density phantom (model 062M by *Computerized Imaging Reference Systems, Inc.)*.

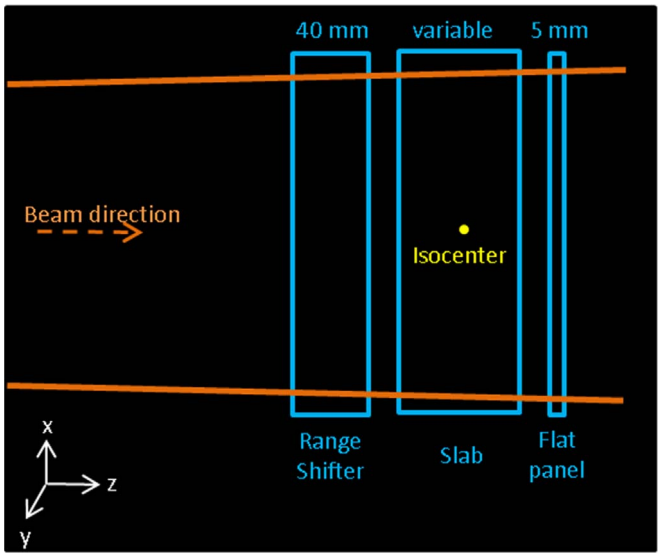

Figure 1. Schematic representation of the simulated elements for FP-PR calibration. The edges of the PR field and the beam direction are depicted in orange. The isocenter is shown in yellow. Three water blocks on the beam path were simulated along the *z*-axis to represent a range shifter, a water equivalent slab of varying thickness and the FP detector. The thickness of each water block is indicated in the schematic.

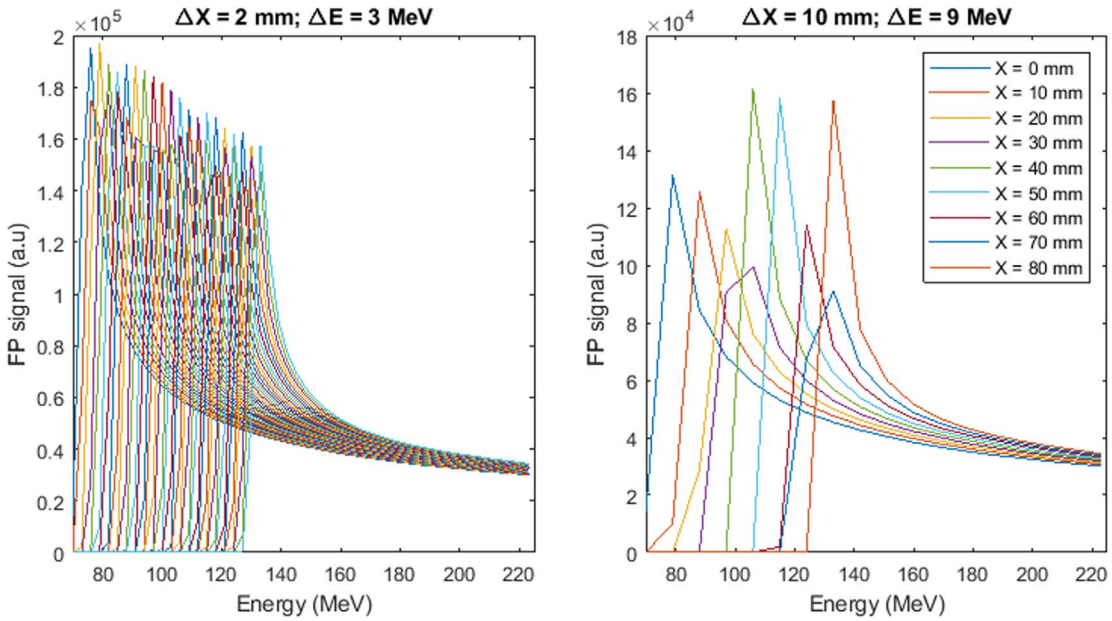

Figure 2. Two calibration datasets, with $\Delta X = 2$ mm and $\Delta E = 3$ MeV (left) and with $\Delta X = 10$ mm and $\Delta E = 9$ MeV (right). ERDFs are represented in different colors, corresponding to thicknesses from 0 to 80 mm. For each plot, the left-most ERDF corresponds to $X = 0$ mm and the right-most ERDF corresponds to $X = 80$ mm. The legend in the left side plot is omitted for readability.

The phantom consists of a large and a small ring, containing 16 inserts of 8 different tissue equivalent materials representing the following tissue types: lung (exhale), adipose, muscle, dense bone, lung (inhale), breast, liver and trabecular bone.

An ERDF was obtained for each pixel in the FP-PR images of the phantom. WEPL values were obtained by minimizing the squared difference between each ERDF in a phantom FP-PR image and the ERDFs in a chosen calibration dataset. To allow comparison between ERDFs in the FP-PR images and ERDFs in the calibration, all ERDFs were normalized over their area. A cubic spline interpolation was applied to all ERDFs with $\Delta E > 1$ MeV, in order to have data points every 1 MeV in all calibration datasets and imaging PR fields. A linear interpolation

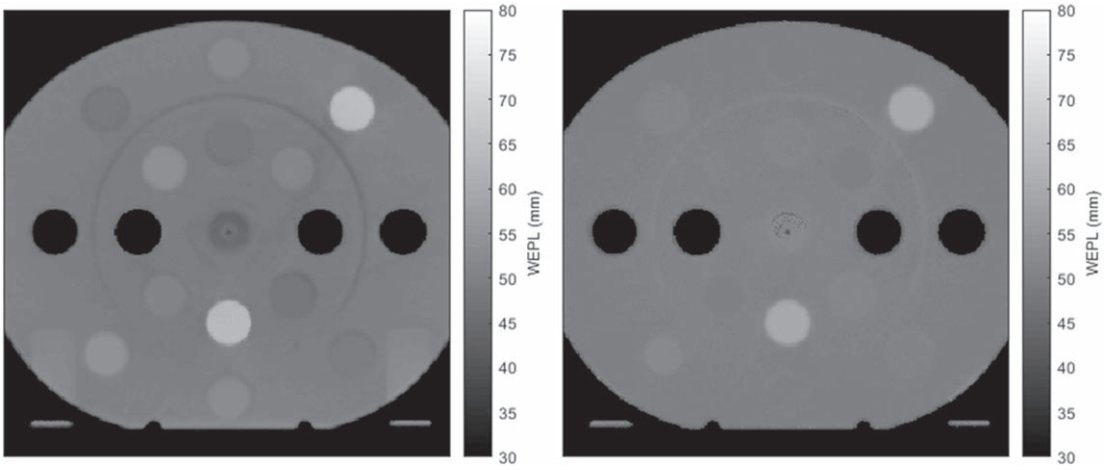

Figure 3. WEPL images in mm resulting from FP-PR simulations using a calibration with $\Delta X = 2$ mm and $\Delta E = 3$ MeV (left) and $\Delta X = 10$ mm and $\Delta E = 9$ MeV (right).

across ERDFs corresponding to slab thicknesses not present in the calibration dataset was performed during the minimization process.

WEPL obtained via MLIC-PR (ground truth)

Ground truth WEPL values were provided by a range probing MLIC simulation (MLIC-PR) performed for each insert of the phantom. In the simulations, the MLIC was represented in the CT image by a water block of 30 cm of thickness at the exit of the phantom in the beam direction. The energy of each range probe was 210 MeV, and an isotropic dose grid of 1 mm was used in all directions. Integral depth dose profiles were obtained by integrating the dose in the dimensions perpendicular to the beam direction. The WEPL value corresponding to each insert was obtained using the Bragg peak pull-back method, with respect to a MLIC simulation in air (Huo *et al* 2019, Harms *et al* 2020).

Calibration assessment

WEPL accuracy was quantified in terms of WEPL relative errors (%), to determine the suitability of each calibration setting. WEPL relative errors between the ground truth WEPL values obtained from MLIC-PR simulations and the values obtained from FP-PR simulations in each insert were calculated (Harms *et al* 2020). In the WEPL images obtained by means of FP-PR, regions of interest of 10 mm were selected to extract the mean WEPL value in each insert.

The mean and standard deviation of the relative WEPL errors across all inserts was reported for images obtained with all calibration settings. Furthermore, the variability of the WEPL accuracy was reported as a function of different ΔX with a fixed ΔE, as well as for varying ΔE with a fixed ΔX.

Results

Thirty WEPL images of the electron density phantom were obtained making use of each calibration setting. Figure 3 shows two example WEPL images, obtained with the two calibration datasets depicted in figure 2.

Figure 4 shows the mean and standard deviations extracted from each WEPL image, corresponding to each calibration setting. Mean and standard deviations are greatest for calibration settings with the largest ΔX and ΔE. Furthermore, figure 4 shows that large deviations are found for large ΔE ($\Delta E = 9$ or 7 MeV), regardless of the selected ΔX.

The lowest mean and standard deviations are found for settings with the smallest ΔX and ΔE. Generally, settings with $\Delta X \leqslant 5$ mm, and $\Delta E \leqslant 5$ MeV show mean values within $\pm 0.5\%$ and standard deviations around 1%.

Figure 5 shows the variability of the mean and standard deviations (error bars) as a function of varying ΔE or ΔX separately. Standard deviations experience a great reduction as a function of decreasing ΔE, with values from -15% to 15% for $\Delta E = 9$ MeV towards values within $\pm 1\%$ for $\Delta E = 1$ MeV. Standard deviations had a moderate reduction as a function of decreasing ΔX, laying from -2% to 1% for $\Delta X = 10$ mm and from -1.2% to 0.5% for $\Delta X = 1$ mm.

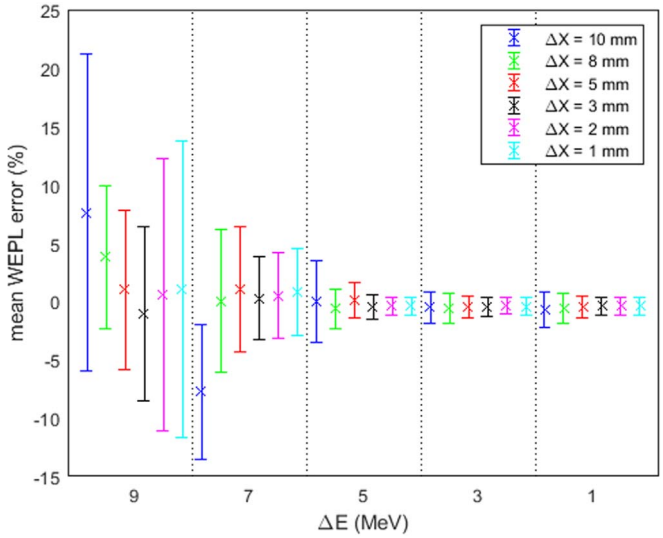

Figure 4. Mean and standard deviation (error bars) of the WEPL relative error (%) for all calibration settings. Different ΔE values are shown across the *x*-axis, and different marker colors stand for different ΔX values.

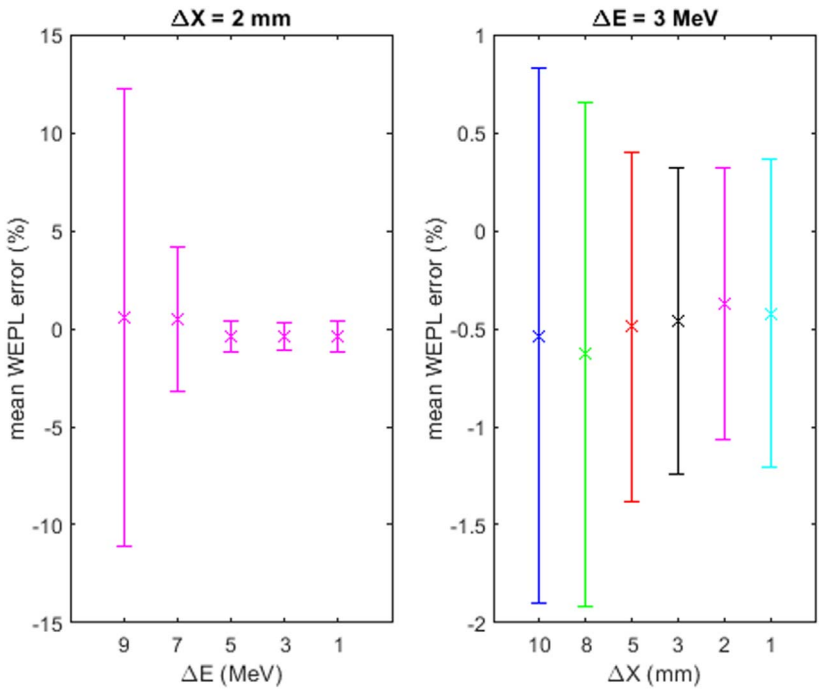

Figure 5. Mean and standard deviation (error bars) of the WEPL relative error (%), as a function of different ΔE values using a fixed $\Delta X = 2$ mm (left side graph), and different ΔX values with a fixed $\Delta E = 3$ MeV (right side graph).

Discussion

The suitability of multiple FP-PR calibration settings was assessed by means of relative WEPL errors, to determine an optimal calibration setting in terms of ΔE and ΔX that enables accurate WEPL measurements. As shown in figure 4, WEPL images of an electron density phantom obtained with $\Delta E \leqslant 5$ MeV and $\Delta X \leqslant 5$ mm resulted in a WEPL accuracy with mean values within $\pm 0.5\%$ and standard deviations around 1%.

Figure 4 shows that WEPL accuracy strongly depends on the sparseness of the calibration dataset (Harms *et al* 2020). WEPL images obtained with the sparsest calibration settings (largest ΔE and ΔX) resulted in the largest deviations, especially for lung and bone equivalent tissue inserts (see table s1 (available online at stacks.iop.org/PMB/66/21NT02/mmedia) and figure s1 in supplementary material). For calibration settings with $\Delta E \leqslant 5$ MeV and $\Delta X \leqslant 5$ mm, relative WEPL errors were reduced across all inserts, although higher relative

Table 1. Cross comparison between the calibration parameters and the achieved WEPL accuracy for lung, soft, and bone tissue equivalent materials in previous FP-PR studies and in this study (Huo *et al* 2019, Harms *et al* 2020).

	Huo *et al*	Harms *et al*	Seller Oria *et al*
Type of study	Simulation	Experiment	Simulation
ΔE (MeV)	<2	4.8	3
ΔX (mm)	1	5–10	5
Lung WEPL accuracy (%)	1.3%	2.65%	−1.1%
Soft WEPL accuracy (%)	−0.2%	−0.14%	−0.4%
Bone WEPL accuracy (%)	−0.5%	0.61%	0.0%

WEPL errors were found in inserts corresponding to lung equivalent tissues with respect to other inserts (see figure s1) (Harms *et al* 2020). Lung equivalent inserts have the lowest densities, meaning that a sub-millimeter absolute WEPL error can result in a relative WEPL error of up to −2.5%. The ground truth WEPL values used to calculate relative WEPL errors were as well obtained with sub-millimeter accuracy, making use of the pull-back method (Farace *et al* 2016a, 2016b, Meijers *et al* 2021).

ΔE and ΔX were investigated separately in figure 5, showing that ΔE has a stronger impact than ΔX in the WEPL accuracy. This is due to the fact that the characteristic steep dose increase in an ERDF gets smoothed out by the cubic interpolation performed within data points in an ERDF (across the energy dimension). In that case, the optimization process in which ERDFs in the calibration dataset are compared against ERDFs from a FP-PR image of the phantom is more inaccurate. On the contrary, ΔX does not show a strong impact on WEPL accuracy. Linear interpolation between ERDFs corresponding to different slab thicknesses is successfully performed since all ERDFs in a calibration dataset have a similar shape.

Mean and standard deviation values are comparable for calibration settings with $\Delta E = 3$ MeV or $\Delta E = 1$ MeV, as well as for settings with $\Delta X = 2$ mm or $\Delta X = 1$ mm. However, a calibration dataset with $\Delta E = 1$ MeV or $\Delta X = 1$ mm would result in a highly time consuming FP calibration dataset acquisition. For practicability, optimal calibration settings within the framework of this study were restricted to $3\text{ MeV} \leqslant \Delta E \leqslant 5\text{ MeV}$ and $2\text{ mm} \leqslant \Delta X \leqslant 5\text{ mm}$.

Table 1 shows a comparison between the WEPL accuracy achieved in other studies against the WEPL accuracy obtained in this study for an exemplary FP calibration setting chosen within the optimality boundaries. Huo *et al* chose small ΔE and ΔX, and obtained a WEPL accuracy similar to the one achieved in this study with $\Delta E = 3$ MeV and $\Delta X = 5$ mm. Harms *et al* opted for an experimental acquisition of a calibration dataset with large ΔX, resulting in larger errors in bone and lung equivalent materials.

The implemented procedure to assign a WEPL value to an ERDF extracted from the FP-PR of the phantom was previously described by other studies (Huo *et al* 2019, Harms *et al* 2020). As shown in table 1, the achievable accuracy between this study and previous studies is comparable.

In this study, an optimal FP calibration procedure in terms of ΔE and ΔX was determined, which is essential to bring PF-PR acquisitions towards a clinical application. However, acquisition time and imaging dose remain as limitations of FP-PR (Harms *et al* 2020). Parameters like the spot spacing, the number of energy layers or the energy range remain to be optimized to preserve high WEPL accuracy while reducing the acquisition time and the imaging dose. In this study, FP-PR fields had energies from 70 to 225 MeV, which resulted in many pencil beams stopping inside the phantom. Therefore, it is imperative to develop a methodology that excludes the lowest energy layers that would get absorbed in a patient (Huo *et al* 2019, Harms *et al* 2020).

Pencil beams in the PR fields directed to the electron density phantom went across homogeneous tissue equivalent materials. However, range mixing will certainly impact FP-PR images acquired for patients, where pencil beams intersect a wide variety of tissues, resulting in ERDFs with a less steep dose increase and a slower dose fall off (Huo *et al* 2019). Range mixing can potentially hamper the optimization process in which ERDFs in the calibration dataset and ERDFs acquired from a patient are compared. Therefore, the performance of the optimization process when ERDFs are subject to range mixing should be investigated. Furthermore, a methodology to include range mixing in the calibration dataset or in the optimization process could be developed, for instance by means of signal deconvolution (Hammi *et al* 2018) or artificial intelligence (van der Heyden *et al* 2021).

In this work, high WEPL accuracy with optimal calibration parameters was achieved by means of FP-PR, which suggests that FP-PR could serve as an online range verification tool. FP-PR could be employed for the detection of setup errors, CT calibration curve errors or anatomical variations. Furthermore, a simultaneous

detection of multiple sources of range uncertainty using FP-PR could be automated and integrated into adaptive proton therapy workflows (Seller Oria *et al* 2020).

Conclusion

An optimal FP calibration procedure in the framework of this study has been established, characterized by 3 MeV $\leqslant \Delta E \leqslant$ 5 MeV and 2 mm $\leqslant \Delta X \leqslant$ 5 mm. Within these boundaries, highly accurate WEPL acquisitions by means of FP-PR are feasible and practical, which could assist future online range verification quality control procedures.

Acknowledgments

This study was financially supported by a grant from the Dutch Cancer Society (KWF research project 11518), called 'INCONTROL- Clinical Control Infrastructure for Proton Therapy Treatments'.

ORCID iDs

Carmen Seller Oria https://orcid.org/0000-0002-0785-2009
Gabriel Guterres Marmitt https://orcid.org/0000-0002-8486-7001
Jeffrey Free https://orcid.org/0000-0002-1573-2613

References

Alaka B G, Bentefour E H, Chirvase C, Samuel D and Teo B K K 2020 Feasibility of energy-resolved dose imaging technique in pencil beam scanning mode *Biomed. Phys. Eng. Express* **6** 65009
Bentefour E H, Schnuerer R and Lu H M 2016 Concept of proton radiography using energy resolved dose measurement *Phys. Med. Biol.* **61** N386–93
Deffet S, Macq B, Righetto R, Vander Stappen F and Farace P 2017 Registration of pencil beam proton radiography data with x-ray CT *Med. Phys.* **44** 5393–401
Doolan P J, Testa M, Sharp G, Bentefour E H, Royle G and Lu H M 2015 Patient-specific stopping power calibration for proton therapy planning based on single-detector proton radiography *Phys. Med. Biol.* **60** 1901–17
Farace P, Righetto R, Deffet S, Meijers A and Vander Stappen F 2016a Technical note: a direct ray-tracing method to compute integral depth dose in pencil beam proton radiography with a multilayer ionization chamber *Med. Phys.* **43** 6405–12
Farace P, Righetto R and Meijers A 2016b Pencil beam proton radiography using a multilayer ionization chamber *Phys. Med. Biol.* **61** 4078–87
Gottschalk B, Tang S, Bentefour E H, Cascio E W and Prieels D 2011 Water equivalent path length measurement in proton radiotherapy using time resolved diode dosimetry *Med. Phys.* **38** 2282–8
Hammi A, Placidi L, Weber D C and Lomax A J 2018 Positioning of head and neck patients for proton therapy using proton range probes: a proof of concept study *Phys. Med. Biol.* **63** 245009
Harms J, Maloney L, Sohn J J, Erickson A, Lin Y and Zhang R 2020 Flat-panel imager energy-dependent proton radiography for a proton pencil-beam scanning system *Phys. Med. Biol.* **65** 145001
Huo W, Zwart T, Cooley J, Huang K, Finley C, Jee K W, Sharp G C, Rosenthal S, Xu X G and Lu H M 2019 A single detector energy-resolved proton radiography system: a proof of principle study by Monte Carlo simulations *Phys. Med. Biol.* **64** 025016
Jee K W, Zhang R, Bentefour E H, Doolan P J, Cascio E, Sharp G, Flanz J and Lu H M 2017a Investigation of time-resolved proton radiography using x-ray flat-panel imaging system *Phys. Med. Biol.* **62** 1905–19
Johnson R P 2018 Review of medical radiography and tomography with proton beams *Rep. Prog. Phys.* **81** 016701
Knopf A C and Lomax A 2013 *In vivo* proton range verification: a review *Phys. Med. Biol.* **58** 131–60
Meijers A, Seller Oria C, Free J, Langendijk Jo A, Knopf A C and Both S 2021 Technical Note: first report on an *in vivo* range probing quality control procedure for scanned proton beam therapy in head and neck cancer patients *Med. Phys.* **48** 1372–80
Mumot M, Algranati C, Hartmann M, Schippers J M, Hug E and Lomax A J 2010 Proton range verification using a range probe: definition of concept and initial analysis *Phys. Med. Biol.* **55** 4771–82
Poludniowski G, Allinson N M and Evans P M 2015 Proton radiography and tomography with application to proton therapy *Br. J. Radiol.* **88** 1–14
Ryu H, Song E, Lee J and Kim J 2008 Density and spatial resolutions of proton radiography using a range modulation technique *Phys. Med. Biol.* **53** 5461–8
Schneider U and Pedroni E 1994 Proton radiography as a tool for quiality control in proton therapy *Med. Phys.* **22** 353–63
Schneider U, Pemler P, Besserer J, Pedroni E, Lomax A and Kaser-Hotz B 2005 Patient specific optimization of the relation between CT-Hounsfield units and proton stopping power with proton radiography *Med. Phys.* **32** 195–9
Seller Oria C, Marmitt G G, Both S, Langendijk J A, Knopf A C and Meijers A 2020 Classification of various sources of error in range assessment using proton radiography and neural networks in head and neck cancer patients *Phys. Med. Biol.* **65** 235009
Souris K, Lee J A and Sterpin E 2016 Fast multipurpose Monte Carlo simulation for proton therapy using multi- and many-core CPU architectures *Med. Phys.* **43** 1700–12
Talamonti C *et al* 2010 Proton radiography for clinical applications *Nucl. Instrum. Methods Phys. Res.* A **612** 571–5
Telsemeyer J, Jakel O and Martisikova M 2012 Quantitative carbon ion beam radiography and tomography with a flat-panel detector *Phys. Med. Biol.* **57** 7957–71

Testa M, Verburg J M, Rose M, Min C H, Tang S, Bentefour E H, Paganetti H and Lu H-M 2013 Proton radiography and proton computed tomography based on time-resolved dose measurements *Phys. Med. Biol.* **58** 8215–33

van der Heyden B, Cohilis M, Souris K, de Freita Nascimento L and Sterpin E 2021 Artificial intelligence supported single detector multi-energy proton radiography system *Phys. Med. Biol.* **66** 105001

Würl M, Gianoli C, Englbrecht F S, Schreiber J and Parodi K 2020 A Monte Carlo feasibility study on quantitative laser-driven proton radiography *Z. Med. Phys.* 1–11

Zhang R, Jee K W, Cascio E, Sharp G C, Flanz J B and Lu H M 2018 Improvement of single detector proton radiography by incorporating intensity of time-resolved dose rate functions *Phys. Med. Biol.* **63** 015030

Zygmanski P, Gall K P, Monroe S Z R and Rosenthal S 2000 The measurement of proton stopping power using proton-cone-beam computed tomography *Phys. Med. Biol.* **45** 511–28